Structure of Sphingomyelin Bilayers: A Simulation Study

S. W. Chiu,* S. Vasudevan,† Eric Jakobsson,* R. Jay Mashl,* and H. Larry Scott†

*Department of Molecular and Integrative Physiology, Department of Biochemistry, University of Illinois at Urbana-Champaign Programs in Biophysics, Neuroscience, and Bioengineering, and Beckman Institute, University of Illinois, Urbana, Illinois; and †Department of Biological, Chemical, and Physical Sciences, Illinois Institute of Technology, Chicago, Illinois

ABSTRACT We have carried out a molecular dynamics simulation of a hydrated 18:0 sphingomyelin lipid bilayer. The bilayer contained 1600 sphingomyelin (SM) molecules, and 50,592 water molecules. After construction and initial equilibration, the simulation was run for 3.8 ns at a constant temperature of 50°C and a constant pressure of 1 atm. We present properties of the bilayer calculated from the simulation, and compare with experimental data and with properties of dipalmitoyl phosphatidylcholine (DPPC) bilayers. The SM bilayers are significantly more ordered and compact than DPPC bilayers at the same temperature. SM bilayers also exhibit significant intramolecular hydrogen bonding between phosphate ester oxygen and hydroxyl hydrogen atoms. This results in a decreased hydration in the polar region of the SM bilayer compared with DPPC. Since our simulation system is very large we have calculated the power spectrum of bilayer undulation and peristaltic modes, and we compare these data with similar calculations for DPPC bilayers. We find that the SM bilayer has significantly larger bending modulus and area compressibility compared to DPPC.

INTRODUCTION

Sphingomyelin (SM) is an important component of many animal cell membranes. Although the biological and evolutionary importance of SM is not established, it is known that SM, along with cholesterol, are key components of the stable, detergent-resistant nanodomains in membranes referred to as *functional rafts* (Simons and Ikonen, 1997; Ahmed et al., 1997; Brown and London, 1998). Rafts have been identified as important membrane structural components in signal transduction (Manes et al., 1999; Aman and Ravichandran, 2000; Xavier et al., 1998; Kawabuchi et al., 2000), protein transport (Rozelle et al., 2000; Cheong et al., 1999; Viola et al., 1999), and sorting of membrane components (Manie et al., 2000; Harder et al., 1998; Sönnichsen et al., 2000; Liao et al., 2001). The mechanism for raft formation in the membrane most likely involves differential miscibility of the various lipids, and preferential association of cholesterol with SM over other membrane lipids (Reitveld and Simons, 1998). Although cholesterol is closely associated with SM in most animal cell membranes, it is important to characterize the thermophysical and structural properties of single-component SM bilayers to better understand the properties of mixed lipid-cholesterol systems.

Sphingomyelin consists generally of a sphingosine base with an 18-carbon chain and a double bond at position 4, attached to a phosphorylcholine fatty acid. The fatty acid chains are generally long and saturated or monounsaturated. In bovine brain SM the most abundant fatty acid chains are 18:0 (42%) and 24:0 (27%), whereas in egg SM the dominant fatty acid is 16:0 (66%) followed by 18:0 (10%); see Ramstedt et al. (1999). Recent reviews of organizational and thermophysical properties of sphingolipid bilayers have summarized properties of these systems with and without cholesterol (Brown, 1998; Maggio, 1994; Koynova and Caffrey, 1995). X-ray and scanning calorimetry experiments established that 16:0 SM exhibits a chain melting phase transition at 40.5°C, very close to the phase transition of dipalmitoyl phosphatidylcholine (DPPC) (Calhoun and Shipley, 1979; Maulik and Shipley, 1996). In a comprehensive study using scanning calorimetry and x-ray diffraction, Maulik et al. (1991) analyzed the thermophysical properties of 18:0 SM at various temperatures and levels of hydration. For the highest hydration levels (>25 wt % HO) 18:0 SM has a chain melting phase transition at 45°C. From electron density profiles and assuming the partial specific volume of 18:0 SM to be the same as that of DPPC (Nagle and Wilkinson, 1978), Maulik et al. (1991) calculate the area per molecule, for full hydration, to be 45 $Å^2$ per molecule at 22°C (below the phase transition temperature) and 55 $Å^2$ per molecule at 55°C (above the phase transition temperature). Koynova and Caffrey (1995) have reviewed thermodynamic data for all experimentally studied sphingolipids. Of interest are the facts that 1), the lipid chain melting transition temperature increases slowly with chain length for saturated SM, from 40.5°C for 16:0 SM to 47.5°C for 24:0 SM; and 2), the insertion of a double C=C bond at position 9 in the acyl chain decreases the phase transition temperature by ~15°C, whereas the same substitution reduces transition temperatures in phospholipids by nearly 50°C (Koynova and Caffrey, 1995).

Early ^{1}H-, ^{31}P- (Schmidt et al., 1977), and ^{14}N- (Siminovitch and Jeffrey, 1981) nuclear magnetic resonance (NMR) studies of small single-lamellar vesicles of SM showed that spin-lattice relaxation rates are lower in the polar and the acyl chain regions in SM, linewidths are greater, and chemical

Submitted March 8, 2003, and accepted for publication August 20, 2003.

Address reprint requests to Hugh L. Scott, Jr., Illinois Institute of Technology, 3101 S. Dearborn, Chicago, IL 60616. Tel.: 312-567-3730; Fax: 312-567-3494; E-mail: scotth@iit.edu.

S. Vasudevan's present address is Dept. of Biochemistry and Molecular Biology, School of Medicine, Southern Illinois University, Carbondale, IL 62901-4413.

0006-3495/03/12/3624/12 $2.00

shifts are broader compared to phosphatidylcholine bilayers. Schmidt et al. (1977) interpret the data as evidence for intramolecular hydrogen between phosphate ester oxygen atoms and H atoms in the amide or hydroxyl moieties of SM. McIntosh et al. (1992) examined structural and thermal properties of bovine brain SM and 24:0 SM using scanning calorimetry and x-ray scattering, and found that the electron density profile of 24:0 SM is indicative of chain interdigitation between the two leaflets due to the large difference in chain length of the two methylene chains. Maulik and Shipley (1996) obtained electron density plots for 16:0 SM, with a peak-to-peak distance of 46.9 Å at 29°C and 44.4 Å at 50°C.

Pressure-area plots of SM monolayers have also been utilized to characterize these systems, complementing studies of SM in vesicles. Li et al. (2000) have carried out a systematic set of experiments using monolayer films of SM with acyl chain lengths from 12 to 26 carbons. At 20°C and 30 dynes/cm surface pressure, Li and co-workers find that 18:0 SM films have an area of 47.2 $Å^2$ per molecule. As chain length increases (decreases) this value decreases (increases). Introduction of an unsaturated bond in the acyl chain significantly increases the area per molecule at the same pressure, e.g., to 59.4 $Å^2$ per molecule for 18:1 SM at 30 dynes/cm and 20°C. Kuikka et al. (2001) have carried out a series of monolayer experiments comparing 16:0 SM with its 16:0 sphingamine analog, containing a saturated sphingamine rather than sphingosine base (DH-SM). They find that DH-SM generally has lower area per molecule than the corresponding SM at given temperature and pressure. Epifluorescence microscopy images showed the presence of large ($\sim$10 μm) domains of condensed lipid in 16:0 SM at low surface pressure. The domains changed in size and structure upon addition of cholesterol.

Despite the documented biological importance of sphingolipids, far less is known about their atomic level structure in bilayers than is known for phospholipids. Atomic level simulations can begin to address this problem. The first molecular dynamics simulation to appear is that of Mombelli et al. (2003). This simulation consisted of a bilayer of 128 16:0 SM molecules plus 2864 waters. As we also report below, intramolecular hydrogen bonds were found in the SM polar region. The purpose of the present article is to describe results of molecular dynamics (MD) simulations of bilayers of 18:0 sphingomyelin (SM) in excess water. The simulated system is $\sim$20 nm in lateral dimensions, making them similar in size to raft microdomains (26 $\pm$ 13 nm; Pralle et al., 2000), and the final MD trajectory after equilibration is 2 ns in length. This length scale allows us to probe molecular structure and whole-bilayer undulations.

METHODS

For all MD simulations and energy minimizations we used GROMACS (Ver. 3.1.4) modeling software (Lindahl et al., 2001). In calculating molecular-mechanics torsion profiles in the course of parameterization, GROMOS96 MD software (van Gunsteren et al., 1996) was used because of its capability of restraining dihedral angles. Standard GROMOS96 energy functions (van Gunsteren et al., 1996) were used in all cases. GAUSSIAN98 (Frisch et al., 2002) was used to calculate ab initio torsional profiles and to optimize molecular structures at the theoretical level B3LYP/6-31G(d,p). Analysis of the properties of the system was done using a combination of GROMACS utilities and our own analysis code.

Fig. 1 shows the structure of 18:0 SM, and the numbering and labeling scheme we used. Table 1 lists the atom labels and their corresponding atom types as defined in the interaction parameter file. A 18:0 SM bilayer of 1600 lipids (800 per leaflet) plus 50,592 SPCE waters was constructed by the following process: an equilibrated dipalmitoyl phosphatidylcholine (DPPC) bilayer of 100 DPPC molecules was converted to 18:0 SM by making the necessary atomic level changes and additions. This system was hydrated at 32 waters per lipid and equilibrated using our previously published procedure of alternating short (100-ps) MD runs with 20,000 configurational bias Monte Carlo (CBMC) steps (Chiu et al., 1999a). The MD runs were carried out at a temperature of 50°C, a surface tension of 46 dynes/cm (Chiu et al., 1995), and a normal pressure of 1 atm. After this system was equilibrated, as judged by stability of the system energy and area per molecule, it was enlarged to a system of 400 SM plus 12,800 waters by replication. The same MD-CBMC procedure was applied to this system for equilibration, and, after this was complete, replication was again used to construct the system of 1600 SM plus 50,592 waters. Energy minimization was run after each enlargement step, and between MD and CBMC runs. For the large system CBMC was not used due to limitations in the current version of the CBMC code. MD simulations for the large system were run with the pressure set at 1 atm anisotropically. The simulation is sufficiently large that changing the boundary conditions from constant surface tension to constant isotropic pressure (zero surface tension) did not change the area per molecule of the system.

Initially, force-field parameters for the phosphocholine polar groups were taken from our DPPC force field (Chiu et al., 1999a,b). Parameters for the sphingosine chain polar groups were taken from the GROMOS96 43A1 parameter set (von Gunsteren et al., 1996). Parameters for saturated hydrocarbon chain atoms were taken from our earlier determination of these quantities by fitting to density and heat of vaporization data for hexane, decane, and pentadecane simultaneously (Chiu et al., 1999b). Parameters for the C=C double-bond carbons were determined from simulations of liquid 5-decene (Chiu et al., 1999b). Cutoffs of 20 Å were employed for van der Waals and electrostatic interactions.

After the large bilayer was equilibrated we undertook a re-examination of the force field for the SM polar region. A Hartree-Fock calculation at the HF/6-31G* level was carried out for the SM molecule (carbons below C19 and C41 were truncated). In the last column of Table 1 we list the partial charges used for SM simulation and those derived from HF calculation. The HF/6-31-G* derived charges on the atoms of the amide and hydroxyl groups are much larger than those adopted from the 43A1 parameter set. We also note that in our previous work (Chiu et al., 1999b) the experimental heats of vaporization ΔH_{vap} for (decane and pentadecane) that we used as target values for parameterization are significantly lower than those listed in the CRC Handbook of Chemistry and Physics (Lide, 1990–1991) and the data from TRC Thermodynamic Tables (Texas A & M University System, College Station, TX). We therefore have also recalculated, following the same procedure as Chiu et al. (1999b), 6–12 parameters for hydrocarbon chains using the new values of the heats of vaporization as targets. Details of parameterization and the force-field parameters for SM used in this work are presented in Appendix.

The simulation was then re-started from the beginning snapshot of the previous 1600 SM simulation, and was run for 1 ns for equilibration, and then another 2.8 ns, the last 2.0 ns of which were used for averaging. The particle-mesh Ewald method was used for the long-range electrostatic corrections. We used a cutoff of 1.0 nm in the direct space and a Fourier spacing of 0.15 nm. A sixth-order interpolation was used. For the van der Waal interactions, a twin-

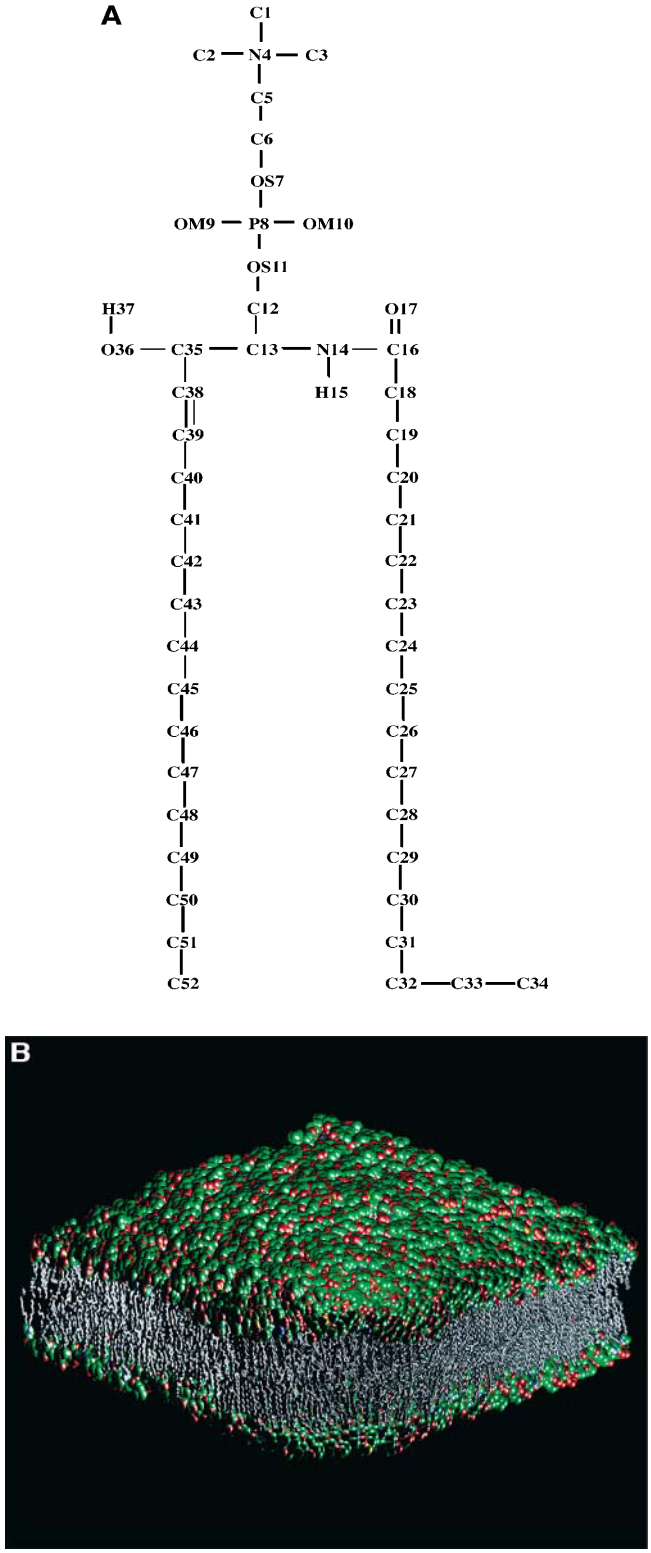

FIGURE 1 (*a*) Single 18:0 SM molecule, showing the atom numbering scheme used. (*b*) Snapshot of the SM bilayer taken near the end of the simulation trajectory. Water molecules are omitted for clarity.

TABLE 1 Atom labels, types, and charges (in units of e^-) for SM and water molecules

Atom label	Atom type	Description	Charge[†]
C1, C2, C3	CH3*	Aliphatic methyl group	0.4 (0.356)[‡]
N4	NL	Choline nitrogen	−0.5 (−0.573)
C5	CH2*	Aliphatic methylene group	0.3 (0.286)
C6	CH2*	Aliphatic methylene group	0.4 (0.365)
OS7	OA	Phosphate ester oxygen	−0.8 (−0.706)
P8	P	Phosphorus	1.7 (1.636)
OM9, OM10	OM	Phosphate oxygen	−0.8 (−0.855)[§]
OS11	OA	Phosphate ester oxygen	−0.7 (−0.711)
C12	CH2*	Aliphatic methylene group	0.25 (0.366)
C13	CH1*	Aliphatic methylidyne group	0.15 (0.265)
N14	N	Amide nitrogen	−0.85 (−0.857)
H15	H	Amide hydrogen	0.45 (0.475)
C16	C0	SP2 bare carbon	0.7 (0.724)
O17	O	Carbonyl oxygen	−0.7 (−0.653)
C18...C33, C40...C51	CH2*	Aliphatic methylene group	0.0
C34, C52	CH3*	Aliphatic methyl group	0.0
C35	CH1*	Aliphatic methylidyne group	0.325 (0.317)
O36	OA	Hydroxyl oxygen	−0.76 (−0.760)
H37	H	Hydroxyl hydrogen	0.435 (0.438)
C38, C39	CH1′	Alkenic methylidyne group	0.0
OW	OW	Water oxygen	−0.8476
HW1, HW2	H	Water hydrogen	0.4238

[†]Values in parentheses are HF/6–31G(d) atomic charges with hydrogens summed into heavy atoms except those with polar hydrogen.
[‡]Averaged charge of the three choline methyl groups.
[§]Averaged charge of the two phosphate oxygens.

range cutoff (1.0/1.6 nm) was applied. The system was run under the NPT condition with semi-isotropic pressure coupling, i.e., pressure coupling which is isotropic in the *x*- and *y*-directions, but different in the *z*-direction (the bilayer normal). The neighbor pairlist was updated every five timesteps. All bond lengths of the lipids were constrained with the LINCS algorithm (Hess et al., 1997). The SETTLE algorithm (Miyamoto and Kollman, 1992) was applied to water molecules for bond length constraint.

Temperature boundary conditions were set using the Nosé-Hoover algorithm (Nosé, 1984; Hoover, 1985). Pressure boundary conditions were set using the Parrinello-Rahman pressure coupling method (Parrinello and Rahman, 1981). The simulation is sufficiently large that changing the boundary conditions from constant surface tension to constant isotropic pressure (zero surface tension) did not change the area per molecule of the system.

Fluctuations of the membrane produce wavevector-dependent undulatory and peristaltic modes (Lindahl and Edholm, 2000). To compute these modes from simulation, we represented the position of each lipid along the membrane normal direction by the *z*-coordinate, of its carbon C13 atom (Fig. 1 *a*). For the undulatory spectrum, the instantaneous fluctuations, $\Delta u_{\mathrm{und}} = z_{\mathrm{i}} - \langle z_{\mathrm{i}} \rangle$, of the lipid positions from their leaflet average, $\langle z_{\mathrm{i}} \rangle$, were calculated. The lipids were then binned into cells according to the positions along the *xy*-plane, and the cell values were defined to be the average of the instantaneous fluctuations of the contributing lipids (each leaflet taken separately). Application of a two-dimensional fast Fourier transform to the cell values provides the undulatory spectral amplitudes and intensities, which were subsequently time-averaged (sampling rate, 0.5 ps) and histogrammed according to wavevector magnitude, q. Note that this method is unreliable at the length scale of individual lipids (toward large q). For the peristaltic spectrum, the instantaneous fluctuations in bilayer thickness, $\Delta h_{\mathrm{per}} = (h - \langle h \rangle)/2$, where h is the distance between corresponding *z*-cells from the monolayers and $<h>$ is the average distance, were analyzed. The calculated Fourier amplitudes $<u^2(q)>$ plotted here are scaled by the area of the system, and the values of the fitting coefficients have been converted to standard units.

RESULTS

Fig. 2 *a* is a plot of the area per molecule versus time for the full 2.8-ns simulation, after equilibration, using the revised force field. The time-average molecular area for the last 2 ns is 53.0 Å^2. Although the area depicted in Fig. 2 *a* has decreased by only ~0.6 Å^2 over 2.8 ns, the simulation time for this raft-size SM bilayer may not be long enough. To conclude, the system will stabilize with a molecular area of ~53 Å^2. However, a plot of the molecular area versus time for a small SM bilayer (100 SM molecules and 3162 waters) over 38 ns, run under identical boundary conditions, as shown in Fig. 2 *b*, shows that the bilayer stabilizes with an average molecular area of ~52 Å^2. These results are in close agreement with the experimental data of Maulik et al. (1991), despite their estimate of 55 Å^2 for the area per molecule; one contribution to the difference between experiment and simulation comes from the Maulik group's assumption that the molecular volume for 18:0 SM is the same as that for DPPC, i.e., 1232 Å^3 (for this, see Nagle and Tristram-Nagle, 2000). From the dimensions of our simulation box, and assuming a molecular volume for water of 30.4 Å^3 (Armen et al., 1998), we find the average molecular volume for an SM in an equilibrated bilayer to be 1182 Å^3. If we use this value of the molecular volume and the *d*-spacing measured by Maulik and Shipley (1996), we find an area per molecule of 52.7 Å^2 for the experimental data, in excellent agreement with the simulation prediction. The low area per molecule for 18:0 SM, above its phase transition temperature, is in contrast to the molecular areas of phospholipids above their transitions (e.g., 64 Å^2 for DPPC; Nagle and Tristram-Nagle, 2000). The relatively low area per molecule indicates that the fluid phase of SM is considerably more ordered than that of phospholipids, a conclusion supported by the small (compared to phosphatidylcholine values) change in enthalpy for sphingomyelins compared to phosphatidylcholine values (a factor of ~2/3; Koynova and Caffrey, 1995).

In Fig. 3 we plot the calculated electron density profile for the bilayer. The peak-to-peak distance is 42.4 Å. By comparison, Maulik et al. (1991) obtain a value of 41 Å for 18:0 SM at 50°C, at all hydration levels between 20 and 50 wt %. Our calculated profile shows methylene ''shoulders'' more distinctively than does the experimental profile. A possible explanation for this is longer time- and length-scale undulation fluctuations in experimental systems, which could ''wash out'' the shoulder locations in an electron density plot.

The chain order parameter profile for 18:0 SM is presented in Fig. 4. Other than the large dip at position 4–5 in the sphingosine chain, both chains are more ordered than are phospholipid chains in the fluid phase, consistent with the observed low value of the area per molecule. Fig. 4 shows that the order parameters for both chains take on values (excluding the double-bonded carbon in the sphingosine chain) of ~0.3 near the top of the chains, and decrease to ~0.1 for the acyl chain and 0.15 for the sphingosine chain at the lowest methylene positions. For comparison, the order parameters for both chains of DPPC at a similar temperature

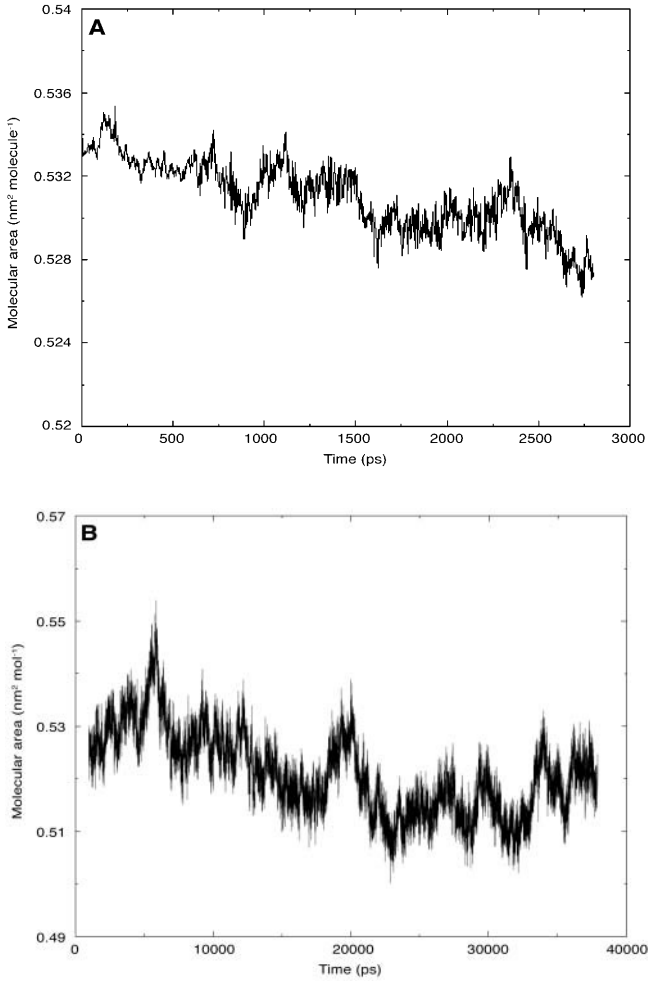

FIGURE 2 (*a*) Plot of area per molecule for the large bilayer versus time over 2.8 ns of simulation. (*b*) Plot of area per molecule for a small SM bilayer (100 SM plus 3162 waters) versus time over a 38-ns simulation.

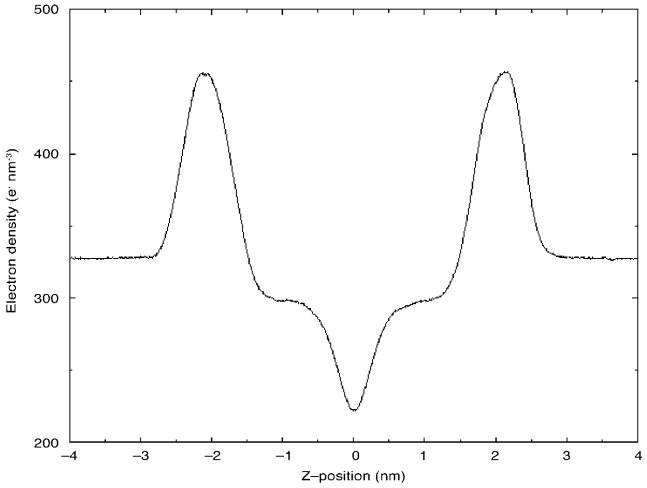

FIGURE 3 Plot of electron density profile for the bilayer.

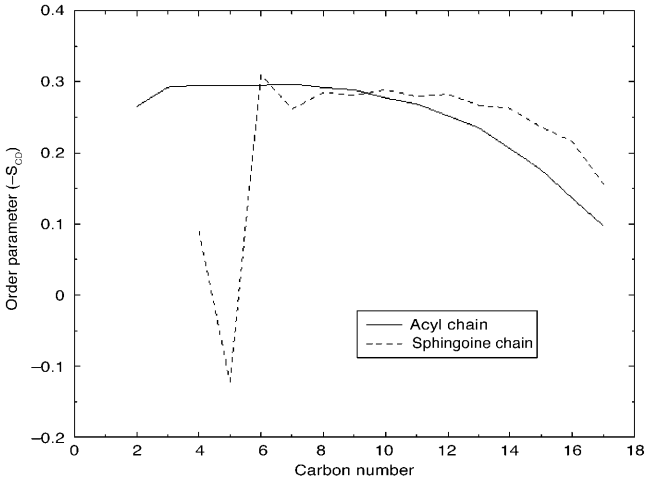

FIGURE 4 Plot of order parameter profiles for the bilayer. (*Solid line*) The acyl chain; (*dashed line*) the sphingosine chain.

begin at ~0.18–0.2 in the upper part of both chains, and are ~0.06 for the lowest methylene (Chiu et al., 1999a).

The source of the different thermophysical behavior of sphingolipids compared to phospholipids is likely the backbone region of the sphingosine chain. In this region there are two polar groups capable of hydrogen-bond formation, an amide and a hydroxyl. We have calculated radial distribution functions (RDF) between pairs of atoms likely to participate in intra- and intermolecular hydrogen bonding. The RDF between atom *x* and atom *y* is defined as the average over all *x*-atoms in the system of the distance from an *x*-atom, and all *y*-atoms up to the interaction range cutoff. The distances between designated atoms on different molecules were binned, and the resulting RDF was normalized by dividing by where *r* is the mid-bin distance variable and *dr* is the bin width, set at 0.01 Å. Fig. 5 shows a plot of the RDF between amide hydrogens and carbonyl oxygens. The sharp peak at ~1.7 Å is due to hydrogen bonding between H15 and O17 on different molecules (for this calculation atoms on the same molecule were excluded). The amide hydrogen is also capable of hydrogen-bonding to neighboring hydroxyl oxygen. Fig. 6 shows the RDF for these atoms, and the 1.75 Å peak reveals hydrogen bonding between these moieties as well.

Also of interest is the possibility of intramolecular hydrogen bonding in SM. The possibility of such bonding was first discussed by Schmidt et al. (1977) to account for chemical shift data in their NMR data. The most likely candidates for participation in intramolecular hydrogen bonding are the phosphate oxygens and the hydroxyl and amide hydrogens. Fig. 7 shows the RDF calculated between the ester oxygen OS11 and the hydroxyl hydrogen, H37. The plot has a very sharp peak at 1.6 Å, which is due to intramolecular hydrogen bonding. This hydrogen bonding is extensive, existing in 57% of the SM molecules in our simulation cell. The implication is that over half of the SM molecules in the bilayer essentially have a six-membered ring (including the hydroxyl hydrogen, H37, and closed by the H37-OS11 hydrogen bond) in the polar regions of their sphingosine chains. Fig. 8 is a plot of the RDF between the ester oxygen OS7 and the hydroxyl hydrogen H37. This RDF has a small, sharp peak at 1.7 Å indicative of some hydrogen bonding but far less than in the case of the OS11 oxygen. Similar RDF values calculated between phosphoryl oxygens (OM9 and OM10) and the hydroxyl hydrogen show almost no intramolecular hydrogen bonding. Table 2 summarizes the hydrogen-bonding data we have found in our simulation, from RDF calculations. Fig. 9 shows a typical SM molecule, with an intramolecular hydrogen bond.

Given the unique and frequent appearance of intramolecular hydrogen bonds in the polar region of SM molecules it is natural to examine the average orientation

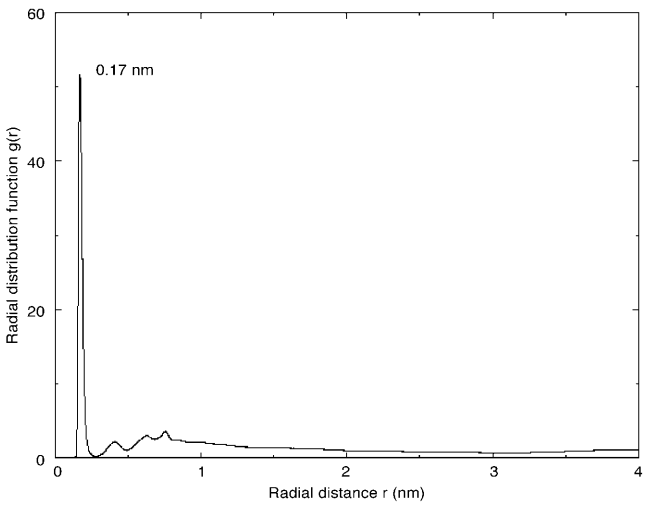

FIGURE 5 Plot of RDF between SM amide hydrogens and carbonyl oxygens.

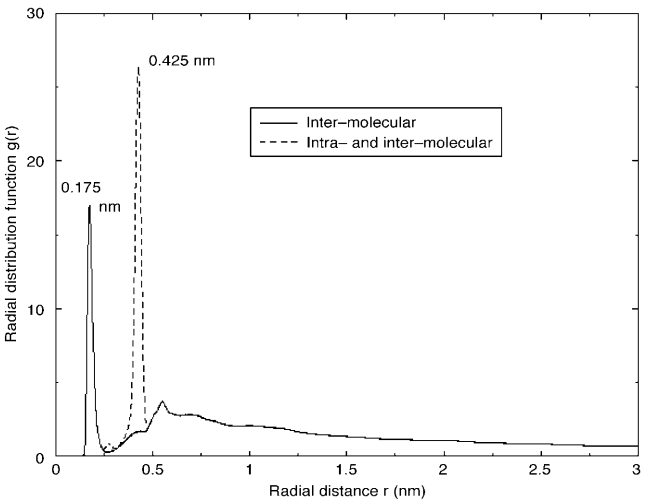

FIGURE 6 Plot of the RDF between amide hydrogen and hydroxyl oxygen.

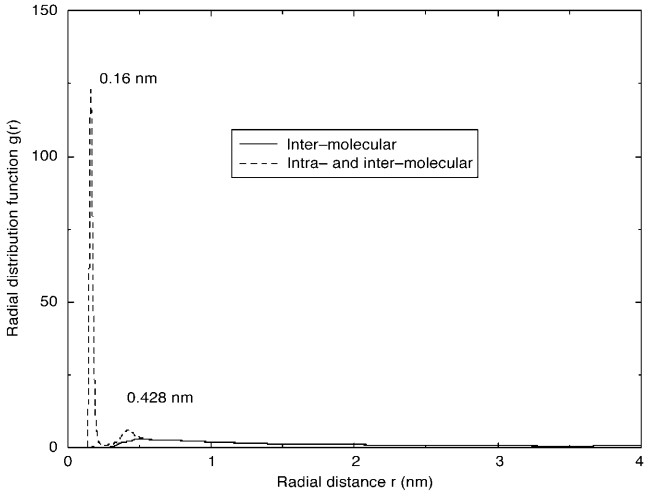

FIGURE 7 Plots of RDF calculated between the ester oxygen, OS11, and the hydroxyl hydrogen, H37.

of the *P–N* dipole in SM bilayers to compare with DPPC bilayers. Fig. 10 is a plot of the angular distribution function for the *P–N* dipole vector. The angle is measured from the bilayer normal so that 90° represents a vector pointing parallel to the bilayer plane. The peak in the plot is at ~90.0° with a width at half-maximum of 61°. Surprisingly, the peak in the *P–N* dipole vector distribution for DPPC bilayers, calculated by Smondryev and Berkowitz (1999) is similarly located, broadly spread between 80° and 90°. For DPPC, however, the distribution of *P–N* dipole vector angles is much wider, ~100°, at half the maximum, compared to SM. We have also calculated the average *P–N* orientation for a DPPC bilayer consisting of 400 DPPC and 12,800 waters (unpublished data; cutoff-based simulation at constant surface tension). We find that the distribution of *P–N* angles again peaks at 80°. But in contrast to Smondryev and

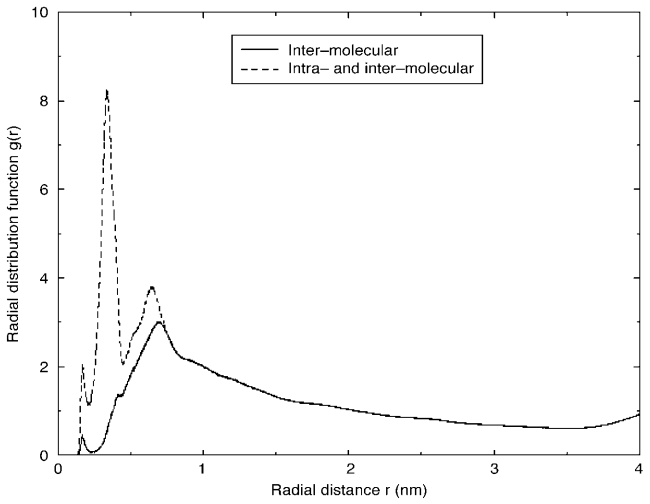

FIGURE 8 Plot of the RDF calculated between the ester oxygen, OS7, and the hydroxyl hydrogen, H37.

TABLE 2 Number of H-bonds per molecule for various donor/acceptor sites

Atom pairs	From RDF	Sites
OM-HW	1.141†	SM-water
OS7-HW	0.487	SM-water
OS11-HW	0.241	SM-water
H15-OW	0.387	SM-water
OA36-HW	0.934	SM-water
H37-OW	0.113	SM-water
O17-H15	0.299	Intermolecular
OA36-H15	0.113	Intermolecular
H37-OS11	0.568	Intramolecular
H37-OS7	0.020	Intramolecular

†Average value for OM9 and OM10 atoms.

Berkowitz we find the width to be narrower than the width of the SM distribution, 52.3°.

The dipole potential for the SM bilayer, shown in Fig. 11, was calculated from the simulations. Consistent with dipole potentials calculated for phospholipids, the large negative contributions from water molecules and large positive contributions from SM polar groups cancel almost everywhere, leaving only a small positive potential barrier of ~287 mV, with the interior of the bilayer positive. The membrane potential (interior of the bilayer relative to the bulk water) was calculated to be 540 mV.

The results of our analysis of the power spectra for undulation and peristaltic bilayer deformation modes are shown in Fig. 12, parts *a* and *b*, respectively. The undulation modes fall into two regimes depending on the wavevector magnitude and are related to the nature of the undulations. In general, the power spectrum for undulation fluctuations is expected to follow the expression (Lindahl and Edholm, 2000),

$$\langle u_{\mathrm{und}}^2(q)\rangle = \frac{k_{\mathrm{B}}T}{A}\left[\frac{1}{k_{\mathrm{c}}q^4 + \gamma q^2} + \frac{1}{\gamma_{\mathrm{p,und}}q^2}\right], \qquad (1)$$

where k_{c} is the bending modulus for undulations, γ is the membrane surface tension, and $\gamma_{\mathrm{p,und}}$ is a molecular protrusion energy density for undulations. Equation 1 admits two regimes,

$$\langle u_{\mathrm{und}}^2(q)\rangle = \begin{cases} \dfrac{k_{\mathrm{B}}T}{A}(k_{\mathrm{c}}q^4 + \gamma q^2)^{-1}, & q < q_0 \\ \dfrac{k_{\mathrm{B}}T}{A}(\gamma_{\mathrm{p,und}}q^2)^{-1}, & q > q_0 \end{cases}, \qquad (2)$$

that are separated by a length scale q_0, related to the bilayer thickness. For small wavenumbers (long wavelengths), the membrane undulations dominate the spectrum, whereas for large wavenumbers (small wavelengths), molecular protrusions are the primary modes. In the latter case, $\gamma_{\mathrm{p,und}}$ is a microscopic surface tension term that is interpreted as a lipid protrusion restoring force per unit area. Lindahl and Edholm (2000) have carried out the same analysis for large (1000 lipids) DPPC.

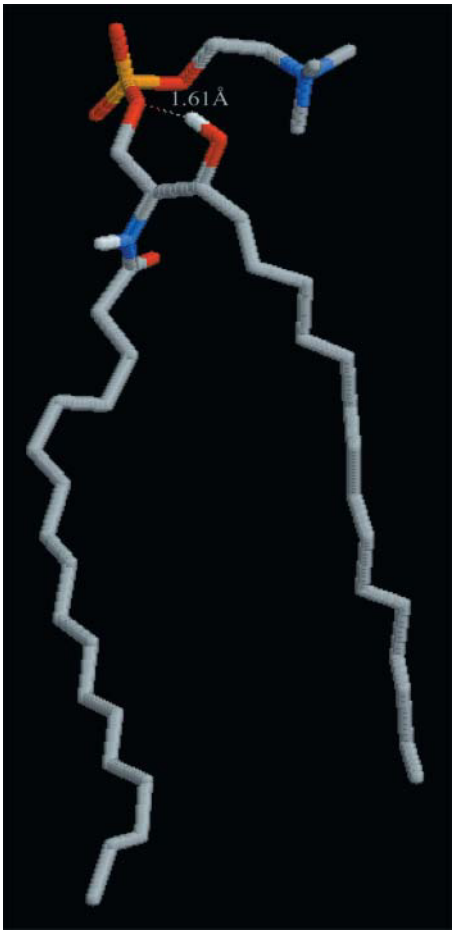

FIGURE 9 Snapshot of an SM molecule with intramolecular hydrogen bond identified.

As did Lindahl and Edholm, we find that the undulation spectral data fall into two linear regimes, corresponding to a $I \propto q^{-4}$ regime in q (small q), and $I \propto q^{-2}$ (large q). Here we have taken the membrane surface tension term in Eq. 2 as zero ($\gamma = 0$) due to the boundary conditions applied in the simulation. We then applied a least-squares fit to each regime independently. From the slope of the small-q line, we obtain a leaflet bending modulus of $k_c = (41.2 \pm 1.9) \times 10^{-20}$ J and lipid restoring force $\gamma_{p,und} = 79$ mN m^{-1}. For comparison, Lindahl and Edholm obtain, for DPPC, $k_c = 4 \times 10^{-20}$ J with $\gamma_{p,und} \approx 50$ mN m^{-1}. The reported experimental value of the bending modulus for DPPC is $k_c = 5 \times 10^{-20}$ J (Evans and Rawicz, 1990). Given the smaller area per molecule, we observe that, in the SM bilayer, it is not surprising that SM bilayers have a larger bending modulus than DPPC bilayers.

The power spectrum for peristaltic modes is presented in Fig. 12 *b*. The peristaltic fluctuation power spectrum is expected to obey the expression (Lindahl and Edholm, 2000)

$$\langle u_{per}^2(q)\rangle = \frac{k_B T}{A}\left[\frac{1}{k_d q^4 + \gamma q^2 + k_e} + \frac{1}{\gamma_{p,per} q^2}\right], \qquad (3)$$

where k_d is the bending modulus for peristaltic motions, k_e is

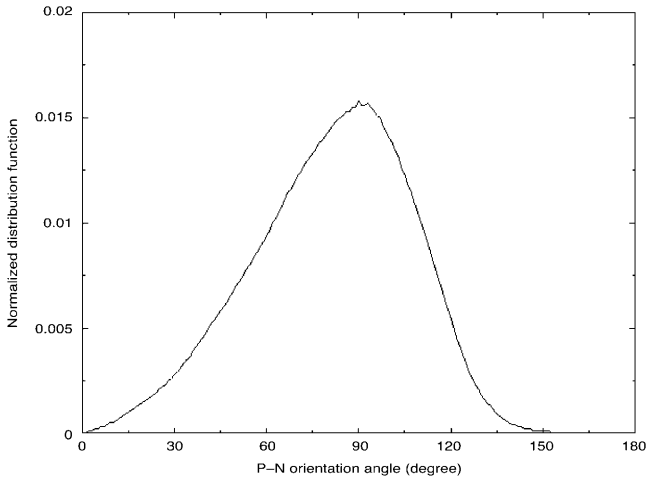

FIGURE 10 Plot of the angular distribution function for the *P–N* dipole vector. The angle is measured from the bilayer normal so that 90° represents a vector pointing parallel to the bilayer plane.

a harmonic restoring force, and $\gamma_{p,per}$ is the restoring force for peristaltic molecular protrusions. In general, $\gamma_{p,per}$ for peristaltic and undulatory molecular protrusions differ. Since the peristaltic modes are limited in amplitude by the thickness of the bilayer, the spectrum is proportional to q^{-2} for large q but becomes asymptotically a constant as q approaches zero. This behavior leads to the two regimes:

$$\langle u_{per}^2(q)\rangle = \begin{cases} \frac{k_B T}{A}(k_d q^4 + \gamma q^2 + k_e)^{-1}, & q < q_0 \\ \frac{k_B T}{A}(\gamma_{p,per} q^2)^{-1}, & q > q_0 \end{cases}. \qquad (4)$$

Setting $\gamma = 0$ and performing a least-squares fit to each regime independently resulted in three converging solutions. In Fig. 12 *b* we show, for clarity, just one of these solutions and obtain the values $k_d = 24 \times 10^{-20}$ J, $k_e = 1.3 \times 10^{-7}$ mN nm^{-3}, and $\gamma_{p,per} = 150$ mN m^{-1}. (The ranges of fitting constants were found to be $k_d = 0.78 \times 10^{-20}$ to 2.4×10^{-20}

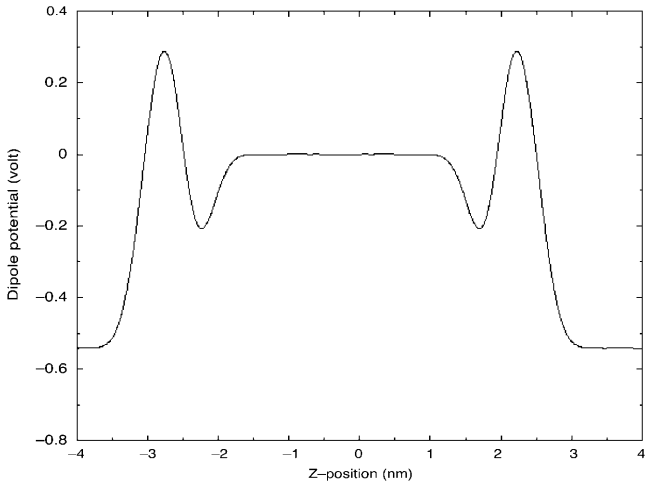

FIGURE 11 Plot of the dipole potential profile for the large bilayer.

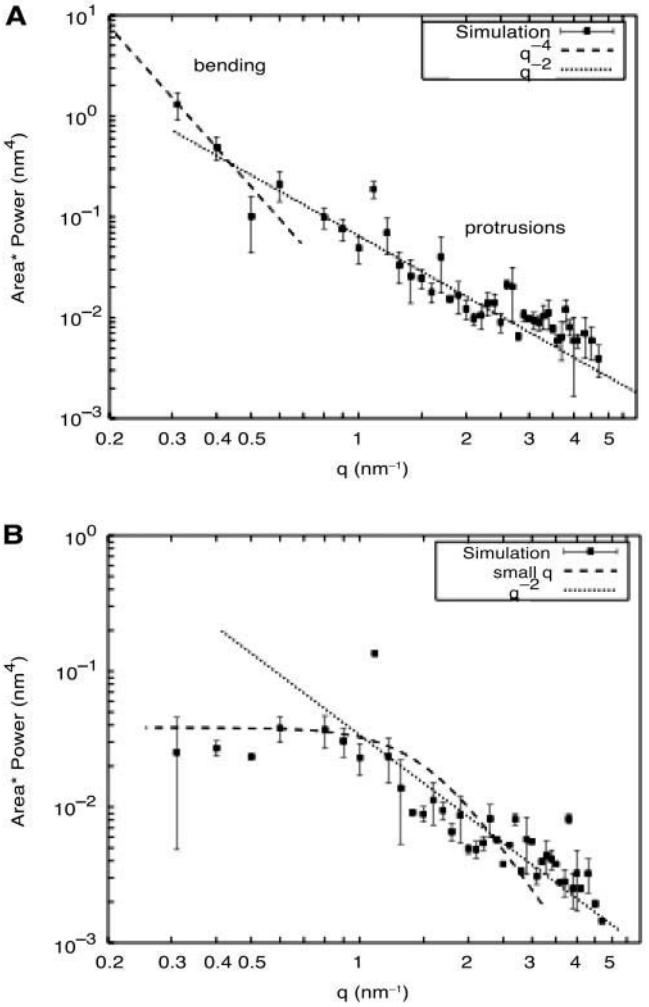

FIGURE 12 Plots of intensity versus wavenumber for (*a*) undulation fluctuations and (*b*) peristaltic fluctuations.

J; $k_e = 1.3 \times 10^{-7}$ to 1.7×10^{-7} mN nm^{-3}; and $\gamma_{p,per} = 84$–165 mN m^{-1}.)

To calculate the area compressibility modulus, K_A, we used ensemble fluctuation theory (Allen and Tildesley, 1987), predicting that $K_A = A(\partial\gamma/\partial A)_T = k_B TA/\sigma_A^2$, where σ_A is the area fluctuation of the system. This calculation includes fluctuations from undulatory and peristaltic modes, and we obtained the value

$$K_A = A(\partial\gamma/\partial A)_T = 4400\,\text{mN m}^{-1}. \quad (5)$$

The large value of the area compressibility modulus underscores the rigid and ordered nature of the SM bilayer, even at the elevated temperature of 50°C. Although there are no experimental data for the compressibility of 18:0 SM bilayers, it is natural to ask whether examination of the more extensive monolayer literature would provide a test of our prediction. We have run simulations of SM monolayers of the same size as individual leaflets for the bilayers discussed here, at a monolayer surface pressure of 30 dynes/cm and at temperatures of 20°C and 50°C (Chiu et al., unpublished data). In that work we have found that area as well as undulation fluctuations for the monolayer are nearly an order-of-magnitude larger than those for the bilayer, although other calculated structural properties are remarkably similar at 50°C. This makes direct comparison of values of K_A unmeaningful.

Since SM bilayers are more ordered, compared to phospholipid bilayers under comparable conditions, and since SM molecules have two chains with different structures, it is natural to examine the question of interdigitation of terminal methyls and near-terminal methylenes between the two leaflets. To this end we calculated atom distributions for each leaflet separately. We found that the distributions of terminal methyls for the two leaflets overlap to an extent that ~23% of all methyls are in the overlap region in the center of the bilayer. We found that only ~2% of all methylenes overlap in the bilayer center. Interdigitation is thus not an important property of the SM bilayer in our simulation.

DISCUSSION

The simulations reported in this article are the largest undertaken to this date, extending the system size to ~400 nm. This size approaches the lower end of estimates for the size of lipid rafts in membranes. Although sphingolipids apparently reside mainly in the outer monolayer of most membranes in which they are found, this study of a hydrated SM bilayer provides atomic level insights into the structure and interactions of SM in membranes. In a subsequent article we will describe simulations of SM monolayers of the same size.

Perhaps the most interesting result of our simulations is the observation that nearly 57% of the SM molecules participate in intramolecular hydrogen bonding between one of the phosphate ester oxygens (primarily OS11) and the hydroxyl hydrogen. This hydrogen bond does not seem to greatly inhibit the conformational freedom of the polar group, as evidenced by the similarity in *P–N* dipole angular RDF for SM and DPPC. The most important consequence of this intramolecular hydrogen bond is that it produces a reduced probability for hydrogen bonding with water, thus reducing the hydration of the polar region. This observation is consistent with a recent experimental study of the hydration state of the interfacial region of DPPC and 16:0 SM vesicles using fluorescence spectroscopy (Nyholm et al., 2003). The higher bending modulus, relative to DPPC, calculated for SM, is consistent with increased inter- and intramolecular hydrogen bonding. The reduced number of hydrogen-bonding sites will also have implications for SM interactions with cholesterol. We have observed significant differences between SM-cholesterol and DPPC-cholesterol interactions in simulations (unpublished data). Inter- and intramolecular hydrogen bonding in SM also implies that the phase transition temperatures of SM bilayers are more dependent on interactions in the polar groups than is the case

for phospholipids. Indeed, the transition temperatures for saturated sphingomyelins do not vary as strongly with acyl chain length as do the transition temperatures for phospholipids.

Given the increased ordering of the hydrocarbon chains, and the restricted polar group mobility from intramolecular hydrogen bonding, it is not unreasonable to expect a reduced molecular volume for SM compared to DPPC. This reduced volume may in fact be responsible for phase separation of sphingolipids from more fluid phospholipids in membranes, which leads to the formation of lipid rafts. The reduced volume also has implications for the interactions of SM with cholesterol, which should not be the same as is found for DPPC (Chiu et al., 2002). This important problem is currently under investigation in our lab.

APPENDIX

United-atom force-field parameters for SM

Wherever possible, we adopted the force-field parameters from GROMOS96 43A1 parameter set (van Gunsteren et al., 1996). Since the charges we adopted for the amide group and the -COH fragment in SM are very different from those used for protein in the 43A1 parameter set, torsional parameters for the dihedral angles involving these atoms were also reparameterized. Our parameter development for atom types CHn*, CH1′, and C0 followed the general methods utilized by several groups (Chiu et al., 1999b; Berger et al., 1997). The procedure outlined by Reiling et al. (1996) was followed to obtain an accurate set of torsional parameters for the dihedral angles involving the atoms of the hydroxyl and amide groups as well as the unsaturated carbon atoms. Some torsional profiles calculated at the B3LYP/6–31G(d,p) level were taken from Langley and Allinger (2002). In this work, the torsional parameters for the dihedral C38–C35–O36–H37 was approximated by fitting to the ab initio torsional profile for isopropanol. Force-field parameters for SM used in this work are presented in Tables A1–A8.

TABLE A1 The normal VDW parameters C_6(i,j) for SM and water; parameters C_6 in 10^{-2} × (kJ mol^{-1} nm^6)

j	O	OM	OA	OW	N
i					
O	0.2261953				
OM	0.2261953	0.2261953			
OA	0.2261953	0.2261953	0.2261953		
OW	0.2433170	0.2433170	0.2433170	0.2617346	
N	0.2347562	0.2347562	0.2347562	0.2525258	0.2436409
NL	0.2347562	0.2347562	0.2347562	0.2525258	0.2436409
H	0.0	0.0	0.0	0.0	0.0
P	0.5773784	0.5773784	0.5773784	0.6210824	0.5992304
C0	0.2643337	0.2643337	0.2643337	0.2843422	0.2743379
CH1*	0.2741026	0.2741026	0.2741026	0.2948504	0.2844765
CH2*	0.4095058	0.4095058	0.4095058	0.4405030	0.4250044
CH3*	0.4542265	0.4542265	0.4542265	0.4886087	0.4714176
CH1′	0.3918183	0.3918183	0.3918183	0.4214766	0.4066474

j	NL	H	P	C0	CH1′
i					
NL	0.2436409				
H	0.0	0.0			
P	0.5992304	0.0	0.1473796		
C0	0.2743379	0.0	0.6747290	0.3089025	
CH1*	0.2844765	0.0	0.6996646	0.3203185	0.3321563
CH2*	0.4250044	0.0	0.1045290	0.4785519	0.4962374
CH3*	0.4714176	0.0	0.1159443	0.5308128	0.5504297
CH1′	0.4066474	0.0	0.1000142	0.4578820	0.4748037

j	CH2*	CH3*	CH1′
i			
CH2*	0.7413727		
CH3*	0.8223353	0.9121396	
CH1′	0.7093509	0.7868166	0.6787123

TABLE A2 The normal VDW parameters C_{12}(i,j) for SM and water; parameters C_{12} in 10^{-5} × (kJ mol^{-1} nm^{12})

j	O	OM	OA	OW	N
i					
O	0.1265625				
OM	0.1265625	0.1265625			
OA	0.1380375	0.2258907	0.1505529		
OW	0.1825875	0.2987943	0.1991421	0.2634129	
N	0.2185875	0.3577063	0.2384061	0.3153489	0.1692601
NL	0.3451500	0.9412624	0.3764436	0.4979364	0.1692601
H	0.0	0.0	0.0	0.0	0.0
P	0.5299874	0.0144534	0.5780397	0.7645953	0.6129011
C0	0.4153612	0.4153612	0.4153612	0.5992279	0.4803422
CH1*	0.5908275	0.5908275	0.5908275	0.852367	0.6832592
CH2*	0.6434887	0.6434887	0.6434887	0.9283398	0.7441590
CH3*	0.5666006	0.5666006	0.5666006	0.8174158	0.6552421
CH1′	0.5755499	0.5755499	0.5755499	0.8303268	0.6655916

j	NL	H	P	C0	CH1*
i					
NL	0.1692601				
H	0.0	0.0			
P	0.6129011	0.0	2.219352		
C0	0.4803422	0.0	1.739348	1.363160	
CH1*	0.6832592	0.0	2.474123	1.939017	2.758141
CH2*	0.7441590	0.0	2.694645	2.111844	3.003977
CH3*	0.6552421	0.0	2.372671	1.859508	2.645043
CH1′	0.6655916	0.0	2.410147	1.888878	2.686821

j	CH2*	CH3*	CH1′
i			
CH2*	3.271726		
CH3*	2.880799	2.536583	
CH1′	2.926301	2.576648	2.617345

Partial charges

The partial charges for the polar region of SM were calculated at the HF/6-31G(d) level using a model SM molecule with truncated hydrocarbon tails

TABLE A3 The third neighbor (1–4) VDW parameters $CS_6^{1/2}(i,j)$ and $CS_{12}^{1/2}(i,j)$ for SM and water; parameters $CS_6^{1/2}$ in (kJ mol^{-1} nm^6)$^{1/2}$, $CS_{12}^{1/2}$ in 10^{-1} × (kJ mol^{-1} nm^{12})$^{1/2}$

Atom type	$CS_6^{1/2}$	$CS_{12}^{1/2}$	Atom type	$CS_6^{1/2}$	$CS_{12}^{1/2}$
O	0.04756	0.8611	OM	0.04756	0.8611
OA	0.04756	1.125	OW	0.05116	1.623
N	0.04936	1.301	NL	0.04936	1.301
H	0.0	0.0	P	0.1214	4.711
C0	0.04838	1.837	CH1*	0.02244	1.2317
CH2*	0.0522	1.880	CH3*	0.0575	2.035
CH1′	0.05	1.000			

TABLE A4 The force-field parameters for the bond terms in SM

Bond in terms of atom types	Force constant, K_{bn} (10^6 mol^{-1} nm^{-4})	Ideal bond length, b_{0n} (nm)
CH3*–NL	8.71	0.147
CH2*–NL	8.71	0.147
CH*n**–CH*n**	7.15	0.153
CH2*–OA	8.18	0.143
P–OM	8.60	0.148
P–OA	4.84	0.161
CH1*–N	8.71	0.147
N–H	18.7	0.100
C0–N	10.2	0.136
C0–O	16.6	0.123
C0–CH2*	7.15	0.152
OA–H	15.7	0.100
CH*n**–CH1′	10.0	0.150
CH1′–CH1′	10.25	0.134

below C19 and C41. The ab initio charge distribution for the choline and phosphate fragments in SM is quite similar to that in DPPC (Chiu et al., 1995). Manual adjustments of the atom charges was performed to maintain the neutrality of the headgroup. The aliphatic and alkenic carbons of the two hydrophobic tails were individually assigned with zero charges. The final charge set used for SM simulation is listed in Table 1.

The van der Waals (VDW) parameters

All were taken from the 43A1 parameter set (van Gunsteren et al., 1996) except those for the atom types CH1*, CH2*, CH3*, CH1′, and C0. Tables A1 and A2 list the normal C_6(i,j) and C_{12}(i,j) parameters, respectively. The 1–4 parameters for third-neighbor interactions are presented in Table A3.

Parameters for the bond and bond angle terms in SM

The parameters for the bond and bond angle types in SM were essentially taken from the 43A1 parameter set. They are listed in Tables A4 and A5, respectively.

TABLE A5 The force-field parameters for the bond angle terms in SM

Bond angle of atom types	Force constant, $K_{\theta n}$ (kJ mol^{-1})	Ideal bond angle, θ_{0n} (degree)
CH*n**–NL–CH*n**	520	109.5
CH1′, CH*n**–CH*n**–NL, N, OA	530	111.0
CH2*–OA–P	530	120.0
OA–P–OM	450	109.6
OA–O–OA	420	103.0
OM–P–OM	780	120.0
CH2*–CH1*–N, CH1*	520	109.5
CH*n**–N–H	505	120.0
CH1′–N–H	480.0	118.0
CH*n**–N–C0	700.0	122.0
N–C0–O	730.0	122.0
N–C0–CH2*	610	115.0
CH2*–C0–O	750	123.0
CH2*–CH2*–CH2*, CH3*	530	111.0
CH1*–CH1*–CH1′	530	111.0
CH2*–CH2*–CH1′	530	112.0
CH*n**–OA–H	450	109.5
CH*n**–CH1′–CH1′	615	126.0

TABLE A6 The force-field parameters for the improper dihedral angle (ξ_n) terms in SM

ξ_n type	ξ_n in terms of atom names	Force constant, $K_{\xi n}$ (kJ mol^{-1} rad^{-2})	Ideal ξ_{0n} (degree)
Planar group	N14–C16–C13–H15	167.42309	0.0
Planar group	C16–C18–N14–O17	167.42309	0.0
Tetrahedral center	C13–N14–C35–C12	334.84617	35.26439
Tetrahedral center	C35–O36–C38′–C13	334.84617	35.26439

TABLE A7 The force-field parameter terms and assignments of dihedral angles in SM

Torsional angle in terms of atom names or types	Force constant, $K_{\phi n}$	Phase shift, cos ϕ_n	Multiplicity, m_n
C3–N4–C5–C6	3.77	+1	3
N4–C5–C6–C7	5.86	+1	3
C5–C6–OS7–P8	3.77	+1	3
C6–OS7–P8–OS11	1.05	+1	3
C6–OS7–P8–OS11	3.14	+1	2
OS7–P8–OS11–C12	1.05	+1	3
OS7–P8–OS11–C12	3.14	+1	2
P8–OS11–C12–C13	3.77	+1	3
OS11–C12–C13–C35	5.92	+1	3
C12–C13–C35–C38	5.92	+1	3
C12–C13–N14–C16	9.75	+1	1
C16–C18–C19–C20	5.92	+1	3
C35–C38–C39–C40	62.7	−1	2
C39–C40–C41–C42	6.75	+1	3
C13–N14–C16–C18	KW_1†		
N14–C16–C18–C19	KW_2†		
C38–C35–C36–H37	KW_3†		
C13–C35–C38–C39	KW_4†		
C38–C39–C40–C41	KW_4†		
CH2*–CH2*–CH2*–CH2*, CH3*	KW_5†		

†*KW* torsion function KW_n is used: $V_{KW}(\psi) = C_0 + C_1 \cos\psi + C_2 \cos^2\psi + C_3 \cos^3\psi$, where $\phi = \psi + \pi$. The coefficients C_n for the KW_n potentials are listed in Table A8.

Parameters for the improper and torsional angles in SM

Table A6 shows the improper dihedral angle ($\square_n$) terms used in SM bilayer simulation. The $\square_n$ values defined for the two tetrahedral centers (the last two rows of Table A6) define the naturally occurring configuration, (2S, 3R) of the sphingosine base. Table A7 lists the proper dihedral angle assignments and their corresponding force-field parameters. Kuwajima-type (Kuwajima et al., 1994; Fang et al., 1999) potential functions are used instead of the normal trigonometric functions for those with force constants KW_n ($n = 1$–5) as listed in column 2 of Table A7. The coefficients C_n for the corresponding *KW* potentials are listed in Table A8.

TABLE A8 The coefficient of KW_n potentials used in SM

KW type	C_0	C_1	C_2	C_3	1–4 Exclusion
KW_1	93.0	−21.0	−72.0	0.0	—
KW_2	3.7585	−6.1733	0.0968	3.5744	C14, O17–C19
KW_3	3.0098	8.1125	0	0	H37–C38, C13
KW_4	4.3488	−13.2311	0.5335	17.0669	C13–C39, C38–C41
KW_5†	7.35	19.40	4.35	−31.10	CH2*–CH2*, CH3*

†From Kuwajima et al. (1994) and Fang et al. (1999).

TABLE A9 Molecular volume (Å^3) and enthalpies of vaporization ΔH_{vap} (kJ mol^{-1}) for hydrocarbon liquids at 298 K

	Molecular volume		ΔH_{vap}	
Liquid	Calculated	Experiment	Calculated	Experiment
Hexane	215.0	218.5†	32.5	31.55†
Decane	319.0	325.3†	51.5	51.37†
Pentadecane	452.9	461.2†	77.0	76.15†
2,3-dimethylbutene	196.4	197.4‡§	31.4	32.53‡
Cis 2-butene	153.0	149.9‡§	22.8	22.16
Cis 2-pentene	181.2	181.1	27.5	26.86
Cis 2-hexene	206.8	203.4§	32.4	32.19
2,5–dimethylhexane	263.9	274.9	36.1	37.9

†Data from TRC Thermodynamic Tables.
‡From Lide (1990–1991).
§Experimental values taken at 293 K.

TABLE A10 The force-field parameters for the bond and bond angle terms in liquid hydrocarbons

Bond type	Force constant (10^6 mol^{-1} nm^{-4})	Ideal bond length (nm)
CH*n**–CH*n**	7.15	0.153
C0–C0	10.25	0.134
CH1′–CH1′	10.25	0.134
CH1′–CH*n**	10.0	0.150
C0–CH*n**	10.0	0.150
Bond angle type	**Force constant (kJ mol^{-1})**	**Ideal bond angle (degree)**
CH*n**–CH*n*–CH*n**	530	111.0
CH*n**–CH1′–CH1′	615	126.0
CH1′–CH*n* –CH*n**	530	112.0
C0–C0–CH3*	615	124.0
CH3*–C0–CH3*	420	112.0

TABLE A11 The force-field parameters for the dihedral angle terms in liquid hydrocarbons

Torsion angle *n* terms of atom types	Force constant (kJ mol^{-1})	Phase shift	Multiplicity
CH*n**–CH*n**–CH*n**–CH*n**	KW_5		
CH1′–CH1′–CH*n**–CH*n**	KW_4		
CH1′–CH2*–CH2*–CH2*, CH3*	7.5	+1	3
CH1′–CH2*–CH2*–CH2*, CH3*	0.5	−1	3

Liquid hydrocarbon properties

Table A9 presents the calculated molar volumes and heats of vaporization of liquid hydrocarbons involving the atom types CH*n**, C0, and CH1′. The respective VDW parameters are from Tables A1–A3. Other bonding parameters used are listed in Tables A10 –A11 . The improper dihedral angle term for planar groups from Table A6 is used for cis conformers of alkenes.

Supported by National Institutes of Health grant GM54651 (to E.J. and H.L.S.), and National Science Foundation and Defense Advanced Research Projects Agency grants (to E.J.). Computer time was provided by the National Center for Supercomputing Applications.

REFERENCES

Ahmed, S. N., D. A. Brown, and E. London. 1997. On the origin of sphingolipid/cholesterol rich detergent-insoluble cell membranes: physiological concentrations of cholesterol and sphingolipid induce formation of a detergent-insoluble liquid-ordered lipid phase in model membranes. *Biochemistry.* 36:10944–10953.

Allen, M. P., and D. J. Tildesley. 1987. Computer Simulation of Liquids. Clarendon Press, Oxford, UK.

Aman, M. J., and K. S. Ravichandran. 2000. A requirement for lipid rafts in B-cell receptor induced Ca^{2+} flux. *Curr. Biol.* 10:393–396.

Armen, R. S., O. D. Uitto, and S. E. Feller. 1998. Phospholipid component volumes: determination and application to bilayer structure calculations. *Biophys. J.* 74:734–744.

Berger, O., O. Edholm, and F. Jahnig. 1997. Molecular dynamics simulations of a fluid bilayer of dipalmitoylphosphatidylcholine at full hydration, constant pressure, and constant temperature. *Biophys. J.* 72: 2002–2013.

Brown, D. A., and E. London. 1998. Functions of lipid rafts in biological membranes. *Annu. Rev. Cell Dev. Biol.* 14:111–136.

Brown, R. E. 1998. Sphingolipid organization in membranes: what physical studies of model membranes reveal. *J. Cell Sci.* 111:1–9.

Calhoun, W. I., and G. G. Shipley. 1979. Sphingomyelin-lecithin bilayers and their interaction with cholesterol. *Biochemistry.* 18:1717–1722.

Cheong, K. H., D. Zachetti, E. Schneeberger, and K. Simons. 1999. VIP17/MAL, a lipid raft-associated protein, is involved in apical transport in MDCK cells. *Proc. Natl. Acad. Sci. USA.* 96:6241–6248.

Chiu, S.-W., M. Clark, S. Subramaniam, H. L. Scott, and E. Jakobsson. 1995. Incorporation of surface tension into molecular dynamics simulation of an interface: a fluid phase lipid bilayer membrane. *Biophys. J.* 69:1230–1245.

Chiu, S.-W., M. Clark, E. Jakobsson, S. Subramaniam, and H. L. Scott. 1999a. Application of a combined Monte Carlo and molecular dynamics method to the simulation of a dipalmitoyl phosphatidylcholine lipid bilayer. *J. Comput. Chem.* 20:1153–1164.

Chiu, S.-W., M. M. Clark, E. Jakobsson, S. Subramaniam, and H. L. Scott. 1999b. Optimization of hydrocarbon chain interaction parameters: application to the simulation of fluid phase lipid bilayers. *J. Phys. Chem. B.* 103:6323–6327.

Chiu, S.-W., E. Jakobsson, R. J. Mashl, and H. L. Scott. 2002. Cholesterol-induced modifications in lipid bilayers: a simulation study. *Biophys. J.* 83:1842–1853.

Evans, E., and W. Rawicz. 1990. Entropy-driven tension and elasticity in condensed-fluid membranes. *Phys. Rev. Lett.* 64:2094–2097.

Fang, Z., D. J. Haymet, W. Shinoda, and S. Okasaki. 1999. Parallel molecular dynamics simulation: implementation of PVM for a lipid membrane. *Comp. Phys. Comm.* 116:295–310.

Frisch, M. J., G. W. Trucks, H. B. Schlegel, G. E. Scuseria, M. A. Robb, J. R. Cheeseman, V. G. Zakrzewski, J. A. Montgomery, Jr., R. E. Stratmann, J. C. Burant, S. Dapprich, J. M. Millam, A. D. Daniels, K. N. Kudin, M. C. Strain, O. Farkas, J. Tomasi, V. Barone, M. Cossi, R. Cammi, B. Mennucci, C. Pomelli, C. Adamo, S. Clifford, J. Ochterski, G. A. Petersson, P. Y. Ayala, Q. Cui, K. Morokuma, N. Rega, P. Salvador, J. J. Dannenberg, D. K. Malick, A. D. Rabuck, K. Raghavachari, J. G. Foresman, J. Cioslowski, J. V. Ortiz, A. G. Baboul, B. B. Stefanov, G. Liu, A. Liashenko, P. Piskorz, I. Komaromi, R. Gomperts, R. L. Martin, D. J. Fox, T. Keith, M. A. Al-Laham, C. Y. Peng, A. Nanayakkara, M. Challacombe, P. M. W. Gill, B. Johnson, W. Chen, M. W. Wong, J. L. Andres, C. Gonzalez, M. Head-Gordon, E. S. Replogle, and J. A. Pople. 2002. Gaussian 98, Rev. A.11.4. Gaussian, Inc., Pittsburgh, PA.

Harder, T., P. Scheiffele, P. Verkade, and K. Simons. 1998. Lipid domain structure of the plasma membrane revealed by patching of membrane components. *J. Cell Biol.* 141:929–942.

Hess, B., H. Bekker, H. J. C. Berendsen, and J. G. E. M. Fraaije. 1997. LINCS: a linear constraint solver for molecular simulations. *J. Comput. Chem.* 18:1463–1472.

Hoover, W. G. 1985. Canonical dynamics: equilibrium phase-space distributions. *Phys. Rev. A.* 31:1695–1697.

Kawabuchi, Y., T. Satomi, Y. Takao, S. Shimonishi, K. Nada, A. Nagai, A. Tarakhovsky, and M. Okada. 2000. Transmembrane phosphoprotein Cbp regulates the activities of Scr-family tyrosine kinases. *Nature.* 404: 999–1002.

Kessel, A., N. Ben-Tal, and S. May. 2001. Interactions of cholesterol with lipid bilayers: the preferred configuration and fluctuations. *Biophys. J.* 81:643–658.

Kuikka, M., B. Ramstedt, J. T. Ohvo-Rekil, and J. P. Slotte. 2001. Membrane properties of *d*-erythro-*n*-acyl sphingomyelins and their corresponding dihydro species. *Biophys. J.* 80:2327–2337.

Koynova, R., and M. Caffrey. 1995. Phases and phase transitions of the sphingolipids. *Biochim. Biophys. Acta.* 1255:213–236.

Kuwajima, S., H. Noma, and T. Akasaka. 1994. Proceedings of the 4th Symposium on Computational Chemistry. Japan Chemistry Program Exchange, Tokyo, Japan. 53.

Langley, C. H., and N. L. Allinger. 2002. Molecular mechanics (MM4) calculations on amides. *J. Phys. Chem. A.* 106:5638–5652.

Li, X.-M., J. M. Smaby, M. M. Momsen, H. L. Brockman, and R. E. Brown. 2000. Sphingomyelin interfacial behavior: the impact of changing acyl chain composition. *Biophys. J.* 78:1921–1931.

Liao, Z., L. M. Cimakasky, D. H. Nguyen, and J. E. Hildreth. 2001. Lipid rafts and HIV pathogenesis: host membrane cholesterol is required for transfection by HIV type 1. *AIDS Res. Hum. Retrovir.* 17:1009–1019.

Lide, D. R. 1990, 1991. CRC Handbook of Chemistry and Physics, 71st Ed. CRC Press, Boca Raton, FL.

Lindahl, E., B. Hess, and D. van der Spoel. 2001. GROMACS 3.0: a package for molecular simulation and trajectory analysis. *J. Mol. Mod.* 7:306–317.

Lindahl, E., and E. Edholm. 2000. Mesoscopic undulations and thickness fluctuations in lipid bilayers from molecular dynamics simulations. *Biophys. J.* 79:426–433.

Maggio, B. 1994. The surface behavior of glycosphingolipids in biomembranes: a new frontier of molecular biology. *Prog. Biophys. Mol. Biol.* 62:55–117.

Manes, S., E. Mira, C. Gomez-Moulton, R. A. Lacalle, P. Keller, J. P. Labrador, and A. C. Martinez. 1999. Membrane raft microdomains mediate front-rear polarity in migrating cells. *EMBO J.* 18:6211–6220.

Manie, S. N., S. Debreyne, S. Vincent, and D. Gerlier. 2000. Measles virus structural components are enriched into lipid raft microdomains: a potential cellular location for virus assembly. *J. Virol.* 74:305–311.

Maulik, P. R., P. K. Sripada, and G. G. Shipley. 1991. Structure and thermotropic properties of hydrated *n*-stearoyl sphingomyelin bilayer membranes. *Biochim. Biophys. Acta.* 1062:211–219.

Maulik, P. R., and G. G. Shipley. 1996. *N*-palmitoyl sphingomyelin bilayers: structure and interactions with cholesterol and dipalmitoylphosphatidylcholine. *Biochemistry.* 35:8025–8034.

McIntosh, T. J., S. A. Simon, D. Needham, and C.-H. Huang. 1992. Structure and cohesive properties of sphingomyelin/cholesterol bilayers. *Biochemistry.* 31:2012–2020.

Mombelli, E., R. Morris, W. Taylor, and F. Fraternali. 2003. Hydrogen bonding propensities of sphingomyelin in solution and in a bilayer assembly: a molecular dynamics study. *Biophys. J.* 84:1507–1517.

Miyamoto, S., and P. Kollman. 1992. SETTLE: an analytical version of the SHAKE and RATTLE algorithms for rigid water molecules. *J. Comput. Chem.* 13:952–962.

Nagle, J. F., and D. A. Wilkinson. 1978. Lecithin bilayers: density measurements and molecular interactions. *Biophys. J.* 23:159–175.

Nagle, F., and S. Tristram-Nagle. 2000. Structure of lipid bilayers. *Biochim. Biophys. Acta.* 1469:159–195.

Nosé, S. 1984. A molecular dynamics method for simulations in the canonical ensemble. *Mol. Phys.* 52:255–268.

Nyholm, T., M. Nylund, A. Soderholm, and J. P. Slotte. 2003. Properties of palmitoyl phosphatidylcholine, sphingomyelin, and dihydrosphingomyelin bilayer membranes as reported by different fluorescent reporter molecules. *Biophys. J.* 84:987–997.

Parrinello, M., and A. Rahman. 1981. Polymorphic transition in single crystals: a new molecular dynamics method. *J. Appl. Phys.* 52:7128–7190.

Pralle, A., P. Keller, E.-L. Florin, K. Simone, and J. K. H. Hörber. 2000. Sphingolipid-cholesterol rafts diffuse as small entities in the plasma membrane of mammalian cells. *J. Cell Biol.* 148:997–1007.

Ramstedt, B., P. Leppimaki, M. Axberg, and P. Slotte. 1999. Analysis of natural and synthetic sphingomyelins using high-performance thin-layer chromatography. *Eur. J. Biochem.* 266:997–1002.

Reiling, S., M. Schlenkrich, and J. Brickmann. 1996. Force field parameters for carbohydrates. *J. Comput. Chem.* 17:456–468.

Reitveld, A., and K. Simons. 1998. The differential miscibility of lipids as the basis for the formation of functional membrane rafts. *Biochim. Biophys. Acta.* 1376:467–479.

Rozelle, A. L., L. M. Machesky, M. Yamamoto, M. H. Driessens, R. H. Insall, M. G. Roth, K. Luby-Phelps, G. Marriott, A. Hall, and H. L. Yin. 2000. Phosphatidylinositol 4,5-biphosphate induces actin-based movement of raft-enriched vesicles through WASP-Arp2/3. *Curr. Biol.* 6: 311–320.

Schmidt, C. F., Y. Barenholz, and T. E. Thompson. 1977. A nuclear magnetic resonance study of sphingomyelin in bilayer systems. *Biochemistry.* 17:2649–2656.

Siminovitch, D. J., and K. R. Jeffrey. 1981. Orientational order in the choline headgroup of sphingomyelin: a ^{14}N-NMR study. *Biochim. Biophys. Acta.* 645:270–278.

Simons, K., and E. Ikonen. 1997. Functional rafts in cell membranes. *Nature.* 387:569–572.

Smondryev, A. M., and M. Berkowitz. 1999. United atom force field for phospholipid membranes. Constant pressure molecular dynamics simulation of DPPC/water system. *J. Comput. Chem.* 20:531–545.

Sönnichsen, B., S. de Renzis, E. Nielsen, J. Reitdorf, and M. Zerial. 2000. Distinct membrane domains on endosomes in the recycling pathway visualized by multicolor imaging of rab4, rab5, and rab11. *J. Cell Biol.* 149:901–914.

van Gunsteren, W. F., S. R. Billeter, R. A. Eising, P. H. Hünenberger, P. Krüger, A. E. Mark, W. R. P. Scott, and I. G. Tironi. 1996. Biomolecular Simulation: The GROMOS96 Manual and User Guide. Hochschulverlag an der ETH Zürich/Biomos, Zürich/Groningen, The Netherlands.

Viola, A., S. Schroeder, Y. Sakakibara, and A. Lanzavecchia. 1999. T-lymphocyte co-stimulation mediated by reorganization of membrane microdomains. *Science.* 283:680–682.

Xavier, R., T. Brennan, Q. Li, C. McCormack, and B. Seed. 1998. Membrane compartmentation is required for efficient T-cell activation. *Immunity.* 6:723–732.